Breakdown of helical edge state topologically protected conductance in time-reversal-breaking excitonic insulators

Yan-Qi Wang,[1,2] Michał Papaj,[1] and Joel E. Moore[1,2]
[1]*Department of Physics, University of California, Berkeley, California 94720, USA*
[2]*Materials Sciences Division, Lawrence Berkeley National Laboratory, Berkeley, California 94720, USA*

(Received 12 June 2023; revised 5 November 2023; accepted 8 November 2023; published 22 November 2023)

Gapless helical edge modes are a hallmark of the quantum spin Hall effect. Protected by time-reversal symmetry, each edge contributes a quantized zero-temperature conductance quantum $G_0 \equiv e^2/h$. However, the experimentally observed conductance in WTe_2 decreases below G_0 per edge already at edge lengths around 100 nm, even in the absence of explicit time-reversal breaking due to an external field or magnetic impurities. In this work, we show how a time-reversal breaking excitonic condensate with a spin-spiral order that can form in WTe_2 leads to the breakdown of conductance quantization. We perform Hartree-Fock calculations to compare time-reversal breaking and preserving excitonic insulators. Using these mean-field models we demonstrate via quantum transport simulations that weak nonmagnetic disorder reproduces the edge length scaling of resistance observed in the experiments. We complement this by analysis in the Luttinger liquid picture, shedding additional light on the mechanism behind the quantization breakdown.

DOI: 10.1103/PhysRevB.108.205420

I. INTRODUCTION

The discovery of the quantum spin Hall (QSH) effect gave rise to a flurry of research on the topological aspects of quantum materials behavior. One of the key features of the QSH is the presence of helical edge states protected by the combination of symmetry and topology [1–9]. The low-energy spectrum of such a system consists of counterpropagating electron states with opposite spins, connected by time-reversal symmetry. Due to the orthogonality of states in a Kramers pair, elastic backscattering by a static potential is forbidden as long as time-reversal symmetry is preserved. When the bulk of the material is insulating, each such helical edge state yields a quantized zero-temperature conductance given by $G_0 \equiv e^2/h$, the conductance quantum. The first QSH insulators to be observed experimentally were HgTe/CdTe quantum well heterostructures, which have been intensively studied [10–27] since the initial proposal [28]. However, because the penetration depth of the edge states in HgTe quantum wells is large, it is often difficult to separate the edge physics from the bulk behavior [29]. This has lead to the search for alternative platforms, among which the most prominent are single layers of the transition metal dichalcogenide WTe_2 in the $1T'$ crystalline structure [30–34]. Several experiments have observed signatures of the QSH effect in that platform, both through transport measurements [31,33] as well as scanning tunneling microscopy/spectroscopy [32,35,36].

Unfortunately, while the edge transport provides a new way towards dissipationless transport and quantum computation [1–9], the experimental observation of robust conductance quantization in realistic scenarios has been elusive [10,11,15,17,31,33,37–39]. For example, in the case of WTe_2, while signs of QSH have been observed up to temperatures of 100 K, these pertain to the devices with edge lengths shorter than 100 nm, much smaller than the multiple-micron lengths for the conductance quantization seen in the integer quantum Hall effect, which also is topological in origin. This discrepancy between the expected robustness of quantization and the imperfect experimental behavior prompted intense theoretical exploration of the possible explanations for this difference. One of the fundamental reasons for the deviation from perfect quantization is that, while the time-reversal symmetry precludes the overlap of wave functions of counterpropagating degenerate time-reversal states, there is no such restriction for them at different energies. Therefore, time-reversal-invariant perturbations can still lead to backscattering of the electrons in a helical channel through interaction-induced inelastic processes with the help of nonmagnetic disorder [40]. In fact, interaction-induced inelastic one- or two-particle backscattering is allowed since the momentum difference between the initial and final states can be compensated by nonmagnetic disorder [41,42]. The deviation of the perfect conductance quanta has been thus attributed to many factors, including coupling to charge puddles [43,44], incoherent electromagnetic noise [9], nuclear spins [45,46], quenched disorder [47,48], spin orbit coupling [49–55], and spin-phonon coupling [56,57].

In this work we explore the possibility of explaining the deviation from the perfect conductance quantization in WTe_2 via the formation of a time-reversal breaking excitonic condensate [58–61]. Besides the quantum spin Hall effect, WTe_2 exhibits also fascinating interaction-driven effects, including superconductivity [62] and potential excitonic insulator states [63–65]. In the latter case, the effect is due to the possible semimetallic noninteracting band structure of WTe_2 with a hole pocket around the Γ point of the Brillouin zone and two electron pockets along the $\Gamma - X$ direction. Formation of an excitonic condensate with finite momentum pairing equal to

the separation between the pockets was postulated and experimental signatures of such a state were observed [64,65]. The impact of exciton condensation on the transport properties of quantum spin Hall phase was previously investigated in the context of electron-hole bilayers of InAs/GaSb described by the Bernevig-Hughes-Zhang model [58,66,67].

However, the exact nature of the excitonic state is unclear and the possibility of time-reversal-breaking spin-spiral or spin-density wave at the Hartree-Fock mean-field level has been raised [60]. Starting from a bulk Hartree-Fock calculation, we observe both time-reversal-breaking and -preserving energy minima, with unconstrained minimization often favoring the former. We then derive a lattice model for the excitonic insulator states and use it to perform quantum transport calculations for a finite width ribbon with disorder. We demonstrate that, while the time-reversal-preserving excitonic insulator is topological and thus exhibits robust conductance quantization of edge state transport, the time-reversal-breaking condensate deviates from e^2/h per edge state conductance in the presence of nonmagnetic static disorder. However, the remnants of the helical edge states, though unprotected from backscattering, remain in the exciton-induced gap and allow us to reproduce the experimentally observed edge-length scaling of resistance, with results close to quantized below 100 nm but with the deviation increasing substantially for longer edges. We then supplement these simulations by analysis in the Luttinger liquid picture, whose relevance to edge transport in WTe_2 has been recently demonstrated experimentally [68]. The second order perturbation theory calculation shows that the combination of scattering from the spin spiral state and nonmagnetic disorder is necessary to introduce backscattering, shedding additional light on the mechanisms that lead to the breakdown of conductance quantization.

II. TRANSPORT FROM THE BULK THEORY

To perform the quantum transport simulations for the excitonic insulator phases of WTe_2, we employ a $k \cdot p$ model as a starting point [65]:

$$H_0(\mathbf{k}) = \left(ak_x^2 + bk_x^4 + 2bk_x^2k_y^2 + b_yk_y^4 + \frac{\delta}{2}\right)I_d + \left(-\frac{\mathbf{k}^2}{2m} - \frac{\delta}{2}\right)I_p + v_xk_x\tau_xs_y + v_yk_y\tau_ys_0, \quad (1)$$

where $\mathbf{k}^2 = k_x^2 + k_y^2$, τ_i and s_i are Pauli matrices in p, d orbitals and spin spaces, respectively, $I_d = (\tau_0 + \tau_z)/2\, s_0$ and $I_p = (\tau_0 - \tau_z)/2\, s_0$ are identity matrices for d and p orbitals, while v_x and v_y determine the spin-orbital coupling. The parameter values we use in the calculations, which were chosen in Ref. [65] in order to reproduce the first principles calculations at low energies, are $a = -3$, $b = 18$, $b_y = 40$, $\delta = -0.9$, $m = 0.03$, $v_x = 0.5$, $v_y = 3$, where all the energies are expressed in eV and lengths in Å. The different value of b_y parameter as compared to Ref. [65] was chosen to ensure that the low energy behavior of the full lattice model is consistent with the continuum model within the cutoff employed therein, with no extra low-energy valley along the $\Gamma - Y$ direction.

We then discretize this Hamiltonian on a rectangular lattice with lattice constants $a_x = 2.805$ Å and $a_y = 6.27$ Å. In discretizing the Hamiltonian we use the finite difference terms up to $(\pm 3, \pm 3)$ hoppings in x and y directions, respectively. At charge neutrality point this system has a hole pocket around Γ point and two electron pockets with minima at $\mathbf{q}_c = \pm 0.32\hat{x}$ along the $\Gamma - X$ direction of the Brillouin zone (see the Appendix for band structure of the model). The value of q_c itself is not exactly commensurate with any crystalline lattice structure and could be affected by effects such as strain and other scenarios that deform the band structure. Based on previous works [60,65], we expect the formation of an excitonic condensate at finite momentum corresponding to the pocket separation q_c in momentum space. When time-reversal symmetry is not enforced, the excitonic order can form either a spin spiral or spin density wave phases, depending on the interaction strength. The lattice constant a_x was therefore chosen such that for q_c as determined for WTe_2 from first principles the resulting order would be commensurate with the discretized lattice with a period increased by a factor of $L_x = 7$. This simplifies expressing the model with a mean-field order parameter in real space. When a finite q order is allowed, the period of the lattice increases correspondingly and the Brillouin zone (BZ) shrinks, while the electron bands are folded into the smaller BZ. We can then label these bands by their corresponding momenta $\mathbf{k}$, spin and orbital index α, and finally the reciprocal lattice vector of the enlarged unit cell $\mathbf{G}_i$, which indicates from which extended Brillouin zone the particular state comes from. In other words, the original momentum $\mathbf{k}_0$ of the state before folding becomes decomposed as $\mathbf{k}_0 = \mathbf{k} + \mathbf{G}_i$.

We then consider Coulomb interaction of the electrons in the lattice model given by

$$H_{\text{int}} = \frac{1}{2N_{k_0}\Omega}\sum_{\mathbf{k}_0,\mathbf{p}_0,\mathbf{q}_0}\sum_{\alpha,\beta} V_{\mathbf{q}_0} c^\dagger_{\mathbf{k}_0+\mathbf{q}_0,\alpha} c^\dagger_{\mathbf{p}_0-\mathbf{q}_0,\beta} c_{\mathbf{p}_0,\beta} c_{\mathbf{k}_0,\alpha}, \quad (2)$$

where Ω is the area of the crystal unit cell, N_{k_0} is the number of momentum points taken in the summation, and $c^\dagger_{\mathbf{k}_0,\alpha}$ are creation operators of a particle with momentum $\mathbf{k}_0$ and α labeling both the orbitals and spin. We assume double-gate screening of the Coulomb potential [69–72], with the resulting Fourier transform

$$V_{\mathbf{q}} = V_0 \frac{\tanh \xi q/2}{\xi q/2}, \quad (3)$$

with $\xi = 250$ Å being the distance between the gates and V_0 the interaction strength parameter. The strength of this interaction can thus be controlled experimentally by either changing the distance between the gates or switching the gate dielectric. We then include the impact of Coulomb interaction at the mean-field level by performing Hartree-Fock calculations. While Hartree-Fock is only an approximate method that is not guaranteed to represent the true ground state of the system, it nevertheless gives insight into the properties of the interacting system. Moreover, in many cases it works surprisingly well when compared to more accurate methods, such as density matrix renormalization group (DMRG), even when considering more strongly correlated systems as compared to the current system under study, for example in the case of moiré heterostructures [73,74]. The Hartree-Fock method is also very convenient for our application in quantum transport

simulations as it results in an effective single-particle Hamiltonian that can be discretized on a lattice, enabling calculation of conductance.

To remain consistent with the previous Hartree-Fock calculations for this model, even though we work with a lattice model, we still maintain the cutoff in momentum summation as in the continuum model of Refs. [60,65], with $|k_x| < 3/2q_c$ and $|k_y| < 0.25$. With the cutoff imposed, we also appropriately rescale the interaction strength parameter to reflect the decreased number of momentum points within the cutoff. We compare the results when we allow for breaking of inversion and time-reversal symmetries during the self-consistent calculation to the case where time reversal is preserved. We choose the interaction strength parameter V_0 so that the rescaled interaction energy within the cutoff at wave vector q_c is $\tilde{V}_{q_c} = 1.71$ eV in the case with time-reversal symmetry enforced and $\tilde{V}_{q_c} = 0.9$ eV otherwise. In expressing the rescaled interaction strength, we follow the convention of Ref. [65]. In both cases we consider the formation of the finite momentum order parameter at $q_c = 0.32$ along x direction as mentioned above. In each self-consistent iteration we diagonalize the quadratic Hamiltonian $H_{\mathrm{MF}} = H_0 + H_{\mathrm{HF}}$ to obtain a set of $n = 4L_x$ eigenvalues $\epsilon_{\mathbf{k}n}$ at each momentum and their corresponding eigenvectors $u_{\mathbf{kG}\alpha n}$, which are n component spinors. These eigenvalues and eigenvectors are then used to obtain the order parameters according to

$$\Delta^{\mathbf{G}_1\mathbf{G}_2}_{\mathrm{H}\alpha\beta} = \delta_{\alpha\beta} \sum_{\mathbf{p}\mathbf{G}n} \frac{V(\mathbf{G}_1 - \mathbf{G}_2)}{N_k} u^*_{\mathbf{pG}-\mathbf{G}_1+\mathbf{G}_2\beta n} u_{\mathbf{pG}\beta n} f_0(\epsilon_{\mathbf{p}n}), \tag{4}$$

$$\Delta^{\mathbf{G}_1\mathbf{G}_2}_{\mathrm{F}\alpha\beta}(\mathbf{k}) = \sum_{\mathbf{p}\mathbf{G}n} \frac{V(\mathbf{p}-\mathbf{k}+\mathbf{G}_1-\mathbf{G}_2)}{N_k} u^*_{\mathbf{pG}-\mathbf{G}_1+\mathbf{G}_2\beta n} u_{\mathbf{pG}\alpha n} f_0(\epsilon_{\mathbf{p}n}), \tag{5}$$

where N_k is the number of points within the cutoff and $f_0(\epsilon) = (e^{\beta(\epsilon-\mu)} + 1)^{-1}$ is the Fermi-Dirac distribution, with $\beta = 1/k_B T$ being the inverse temperature and μ the chemical potential.

The order parameters given by the formulas above represent all the possible couplings between orbital and spin degree of freedom for states separated in momentum by integer multiples of q_c. In particular, some of them represent formation of excitonic order with center of mass momentum q_c. All of these order parameters enter the mean-field Hamiltonian through

$$H_{\mathrm{HF}} = \sum_{\mathbf{k},\alpha,\beta} \sum_{\mathbf{G}_1,\mathbf{G}_2} \left[\Delta^{\mathbf{G}_1\mathbf{G}_2}_{\mathrm{H}\alpha\beta} - \Delta^{\mathbf{G}_1\mathbf{G}_2}_{\mathrm{F}\alpha\beta}(\mathbf{k})\right] c^\dagger_{\mathbf{kG}_1\alpha} c_{\mathbf{kG}_2\beta}. \tag{6}$$

The new H_{MF} is then again diagonalized and the whole procedure is repeated until convergence is achieved, which is monitored by the change in the average value of the order parameters $\Delta^{\mathbf{G}_1\mathbf{G}_2}_{\mathrm{H}\alpha\beta}$ and $\Delta^{\mathbf{G}_1\mathbf{G}_2}_{\mathrm{F}\alpha\beta}(\mathbf{k})$, with the calculation ending when the difference between each step is smaller than 10^{-14}.

The appearance of various excitonic phases is established by calculation of several different quantities. The overall presence of excitonic condensate with $\mathbf{q}_c$ momentum is determined through [60]:

$$\Delta_{\mathrm{exc}} = \sqrt{\frac{1}{N_k} \sum_{\mathbf{kG}\alpha\beta n} |u^*_{\mathbf{kG}\alpha n} u_{\mathbf{kG}+\mathbf{q}_c\beta n} f_0(\epsilon_{\mathbf{k}n})|^2}. \tag{7}$$

The time-reversal-breaking spin spiral and spin density wave components are characterized using the Fourier components of spin density that correspond to the $\mathbf{q}_c$ ordering vector [60]:

$$\rho^s_i = \frac{1}{N_k \tilde{\Omega}} \sum_{\mathbf{k}\sigma\sigma' an} s_{i,\sigma\sigma'} u^*_{\mathbf{k0}\sigma an} u_{\mathbf{kq}_c\sigma' an} f_0(\epsilon_{\mathbf{k}n}), \tag{8}$$

with $\tilde{\Omega} = \Omega A_{BZ}/A_c$ being the area of the crystal unit cell Ω rescaled by the ratio of the Brillouin zone A_{BZ} and area within the cutoff A_c. Expressing the spin density as a vector $\boldsymbol{\rho}^s$ we can then give the expressions that separate the spin spiral and spin density wave components:

$$\rho^{\mathrm{SDW}} = \sqrt{2|\boldsymbol{\rho}^s \cdot \boldsymbol{\rho}^s|}, \quad \rho^{\mathrm{SS}} = \sqrt{2|\boldsymbol{\rho}^s|^2} - \rho^{\mathrm{SDW}}. \tag{9}$$

The exact phase obtained as the Hartree-Fock ground state depends on several factors, most important of which is the screened interaction strength V_0. This parameter is determined by the device configuration, in particular the spacing between the metallic gates that are used to control charge density within the device and the gate insulator material itself. Through the self-consistent calculation we obtain results in agreement with the previous calculations with [65] and without [60] time-reversal symmetry, reproducing the phase diagram that contains spin spiral and spin density wave in the latter case. Representative examples of mean-field band structures are presented in Fig. 1. In panel (a) we show that when time-reversal symmetry is enforced, the exciton condensate forms and the gap opens up, but the bands remain doubly degenerate. The state is topological in nature as will be explicitly demonstrated by the presence of the edge states. In panel (c), the band structure for the time-reversal-breaking state is shown. Again, the exciton condensate formation leads to gap opening, but now the band degeneracy in the proximity of the gap is lifted due to the formation of the spin spiral state. As this degeneracy lifting is small, the system will still retain some of the quantum spin Hall effect features, but will no longer be robust to perturbations.

For the purpose of quantum transport simulation with disorder we need to convert these Hamiltonian terms to their real space counterparts. While the unit cell of the original lattice Hamiltonian consisted of a single site with four spin orbitals, when excitonic order with finite q arises, the unit cell has to increase correspondingly to allow for the spatial modulation of the charge and spin densities. Since we have chosen the lattice constant so that the postulated excitonic order wave vector is commensurate with the original lattice, we can simply extend the original model by including L_x sites in the extended unit cell. The chosen value of $L_x = 7$ enables a reasonable approximation for the modulation of densities within the unit cell while keeping the computational complexity in check. At the same time, we can easily convert the Hartree-Fock order parameters to real space hoppings. As a result of a Fourier transform with $c^\dagger_{\mathbf{k}\alpha} = 1/\sqrt{N} \sum_{\mathbf{r}_i} e^{i\mathbf{k}\cdot\mathbf{r}_i} c^\dagger_{\mathbf{r}_i}$, we obtain hoppings between $\mathbf{r}_i$ and $\mathbf{r}_j$ sites of the lattice:

$$\Delta_{\alpha\beta}(\mathbf{r}_i, \mathbf{r}_j) = \sum_{\mathbf{k}\mathbf{G}_1\mathbf{G}_2} \Delta^{\mathbf{G}_1\mathbf{G}_2}_{\alpha\beta}(\mathbf{k}) e^{i\mathbf{k}\cdot\mathbf{r}} e^{i[(\mathbf{G}_1-\mathbf{G}_2)\cdot\mathbf{r}_j + \mathbf{G}_1\cdot\mathbf{r}]}, \tag{10}$$

where $\Delta^{\mathbf{G}_1\mathbf{G}_2}_{\alpha\beta}(\mathbf{k}) = \Delta^{\mathbf{G}_1\mathbf{G}_2}_{\mathrm{H}\alpha\beta} - \Delta^{\mathbf{G}_1\mathbf{G}_2}_{\mathrm{F}\alpha\beta}(\mathbf{k})$ and $\mathbf{r} = \mathbf{r}_i - \mathbf{r}_j$. Similar to the discretization of the continuum model, we use

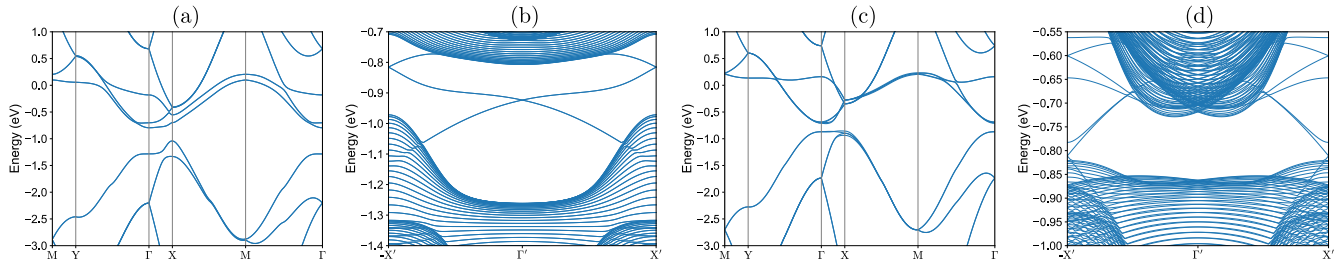

FIG. 1. Band structures of the excitonic condensate systems within Hartree-Fock mean-field approximation. (a) 2D lattice model with time-reversal symmetry preserved. The gap is opened by the exciton formation, but the bands remain doubly degenerate due to symmetry preservation. (b) Spectrum of system from (a) placed on a quasi-1D ribbon. The system is topological, which results in the presence of helical edge states within the excitonic band gap. (c) 2D lattice model with time-reversal symmetry broken. The excitons open the gap, but the spin degeneracy is lifted due to formation of the spin spiral state. (d) Spectrum of system from (c) placed on a quasi-1D ribbon. Even though time reversal is broken, as the magnitude of symmetry breaking terms is relatively small, the remainder of the helical edge states remain in the gap.

hoppings up to $(\pm 3, \pm 3)$ in x and y directions. While the Fourier decomposition of $\Delta_{\alpha\beta}^{\mathbf{G}_1\mathbf{G}_2}(\mathbf{k})$ includes an infinite number of $\Delta_{\alpha\beta}(\mathbf{r}_i, \mathbf{r}_j)$, in practice for the system under study such a limited number of terms reproduces the Hartree-Fock potential with sufficient accuracy, partially due to the choice of lattice constant that results in an order that is commensurate with the initial lattice.

With a real-space model defined as above, we can now set up the quantum transport simulation to study the effect of the time-reversal-breaking excitonic condensate on the helical edge states of the quantum spin Hall state. To perform all the quantum transport calculations we use the KWANT package [75]. The procedure is as follows: the starting point is the two-dimensional model of WTe_2 from Eq. (1) with Hartree-Fock terms that describe the excitonic condensate as given by Eq. (6), which has the band structure represented in either Figs. 1(a) or 1(c), depending on the parameter set. We then restrict this model expressed in real space to a ribbon with a finite width in y direction, establishing hard walls at the boundaries. This means we retain the translational invariance in the x direction, along the spin density modulation coming from the spin spiral state. Due to this translational invariance we can still label the quantum states by their momentum in x direction and calculate the spectrum within the 1D Brillouin zone (which is indicated by primes in the labeling) of the ribbons. Such spectra are presented in Figs. 1(b) and 1(d), both for time-reversal-preserving and -breaking cases. The lines in these panels represent the transverse electronic modes of the ribbon, which are responsible for carrying the electrical current through the sample if they are crossing the Fermi level. Thus the transverse modes that cross the Fermi level form the basis for the scattering matrix that describes transmission of these modes through the region under study. In panel (b), the time-reversal-preserving case, the helical edge states resulting from the topological nature of the excitonic insulator are clearly visible. However, in panel (d) even though the time-reversal symmetry is broken, the remainder of helical edge states is still visible in the gap. These states are partially gapped, but because the magnitude of symmetry breaking terms is not large, there are energy windows within the gap for which a pair of edge states is present and in the absence of any disorder they would contribute $2e^2/h$ to the longitudinal conductance of the ribbon.

In a standard Landauer-Buttiker calculation fashion, we attach the semi-infinite leads to the opposite ends of the ribbon that extend in the x direction. We then introduce additional random on-site potential to the lattice model within the central scattering region to model the disorder that preserves time-reversal symmetry:

$$H_{\text{dis}} = \sum_{\mathbf{r}_i,\alpha} U(\mathbf{r}_i) c^\dagger_{\mathbf{r}_i,\alpha} c_{\mathbf{r}_i,\alpha}. \tag{11}$$

The random on-site values $U(\mathbf{r}_i)$ are taken from a uniform distribution over the range $[-U_0/2, U_0/2]$, where we call U_0 the disorder strength. We calculate the scattering matrix of the system for $n_{\text{avg}} = 100$ independent disorder realizations and then average the conductances over these realizations. In the usual circumstances, the quantum spin Hall edge states are robust with regards to such a disorder and the breakdown of the quantized sample conductance happens only for extremely large disorder strengths. This remains true even in the presence of the excitonic condensate which preserves time-reversal symmetry, as demonstrated in Fig. 2(a). The conductance remains precisely quantized for much of the investigated disorder strength range and the leading source of the quantization breakdown is the coupling between the opposite edges of the sample. This is evident as the conductance curve is sensitive to the width of the ribbon (see the Appendix), with the disorder strength needed to decrease the conductance increasing for wider ribbons. At the same time, when disorder is chosen within the quantized plateau, the result does not depend on the length of the ribbon, revealing the robustness characteristic of the topological transport. Moreover, the variance displayed among the different disorder realizations shows that conductance in that case is very unstable, being dependent on whether the disordered potential forms a path connecting to the opposite edge. Note that, while strong disorder in the bulk of the sample may act to reduce the excitonic order parameter, the gap in the bulk means that weak disorder does not qualitatively modify the phase, unlike at the gapless edge. As long as the bulk gap remains nonzero, we expect the edge treatment here and in the following section to be applicable.

However, once the time-reversal symmetry breaking excitonic condensate is formed, even a small scalar disorder causes a deviation from the perfect value, as exemplified in

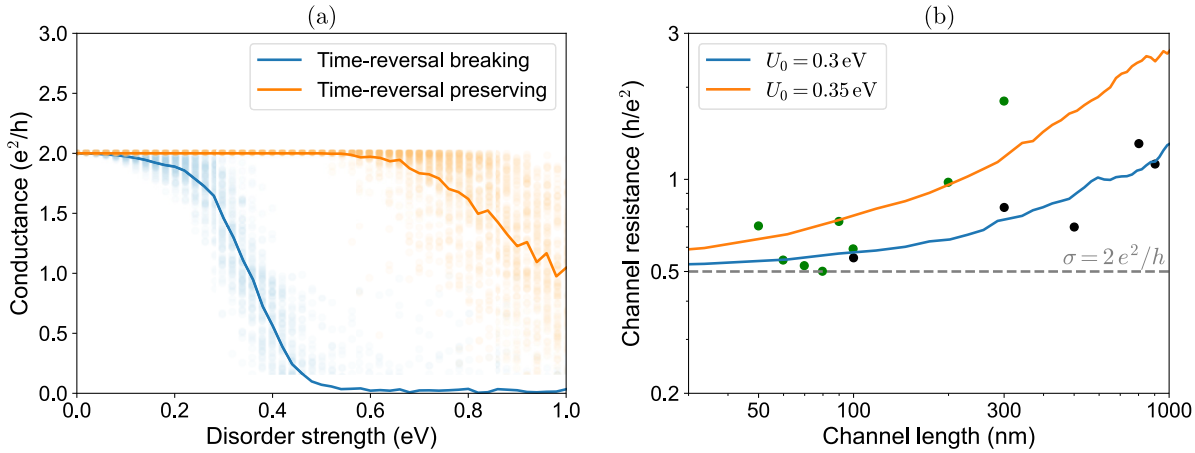

FIG. 2. Quantum transport simulation results. (a) Disorder strength U_0 dependence of conductance for the case of time-reversal-breaking and -preserving exciton condensates. The solid lines show average over 100 disorder realizations, with each realization shown as a separate set of points. In both cases the length of the ribbon is 200 nm and the width is 50 nm. (b) The comparison between the experimental data as reported in [33] and quantum transport simulation in the time-reversal-breaking case averaged over disorder realizations. The experimental data from two different devices and channel lengths 50–1000 nm demonstrates increasing channel resistance for longer edge channels, suggesting lack of topological protection of the quantum spin Hall edge states. This observation is consistent with the simulation result, which can reproduce the observed length dependence and sample variation with relatively small changes to disorder strength value U_0.

Fig. 2(a). In contrast to the time-reversal-preserving case, the decrease from $2e^2/h$ value is immediate. Moreover, the disorder strength dependence is insensitive to the width scaling, indicating that the backscattering processes occur within the same edge. The variance among disorder realizations is also much smaller than previously, confirming that the backscattering is not dependent on the accidental appearance of a pathway across the device. At the same time, increasing the length of the ribbon decreases the conductance for all disorder strengths, revealing the lack of the topological protection.

To further demonstrate this, and to relate our simulations in the time-reversal-breaking case to the experimental data, we calculate the channel resistance of the edge states with increasing ribbon length, keeping all the other Hamiltonian parameters, including the disorder strength U_0, constant. The results are presented in Fig. 2(b), where a comparison between the simulation and experimentally obtained resistance values [33] is made. The experimentally studied edge lengths range from 50 to almost 1000 nm, which we also use as the ribbon lengths in our calculations. While making the comparison, we have to consider that obtaining the edge length scaling of resistance in a single device is nontrivial and requires measurements between multiple different sets of contacts. Resistance measured for each pair thus strongly depends not only on the properties of the edge, but on the quality of each of the contacts as well. Moreover, the experimental data is gathered for one particular disorder realization, which cannot be determined to be the input of our simulation. Therefore, we make the comparison with simulations averaged over multiple disorder realizations and compare the general trends in the data. We include calculations with two different, but comparable disorder strengths. The smaller value $U_0 = 0.3$ eV reproduces the device data represented by the black points quite well, while the larger disorder strength $U_0 = 0.35$ eV reproduces the trend for the device represented by the green points. This demonstrates that the variability between the devices can be explained by a relatively small change in disorder strength that can realistically be expected in experimental conditions. While we cannot obtain a perfect fit to the experimental data (the nonmonotonicity in the data in particular would require knowing more about the disorder pattern and contact quality), the general trends are well explained using realistic material parameters. In both cases, the simulations mirror the experimental data for almost two orders of magnitude in channel length, suggesting that the breakdown of quantization of edge conductance as observed in WTe_2 could be explained by a bulk time-reversal-breaking excitonic condensate.

III. TRANSPORT FROM THE EDGE THEORY

To better understand the mechanism behind the breakdown of quantization in the presence of the time-reversal-breaking excitonic condensate, we use an analytical model based on the Luttinger liquid picture. Such a model can be applied to study the helical edge states that arise in the quantum spin Hall (QSH) insulator under open boundary conditions. The helical edge state consists of two degenerate counterpropagating electron states with opposite spins, related by the time-reversal symmetry, each contributing a quantized zero temperature conductance $G_0 \equiv e^2/h$ in opposite directions. Even though the quantized conductance G_0 is protected by time-reversal symmetry, there exists a multitude of proposals that can explain the breakdown of the quantization as discussed in the Introduction. In terms of time-reversal-breaking mechanisms, previous works suggested backscattering from magnetic impurities as one of the most prominent. However, in many systems such as WTe_2 the source of such impurities is not obvious and thus we look towards a different, intrinsic source of time-reversal breaking, namely the excitonic condensate. In this section, following Refs. [40,45,46], we compute the two terminal conductance for a QSH insulator slab with bulk spin spiral order. While in the referenced works the justification for

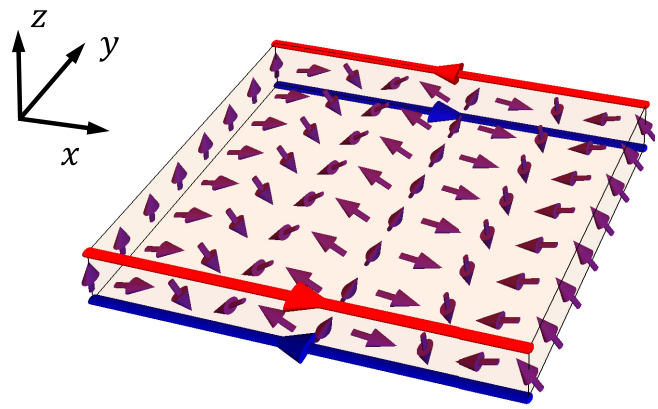

FIG. 3. Illustration of spin spiral order in the quantum spin Hall phase. The single layer of WTe_2 (orange cuboid) is in a quantum spin Hall effect phase before the appearance of the bulk spin spiral order (purple arrows). The red and blue arrows on the boundary stand for the helical edge states from the original quantum spin Hall effect.

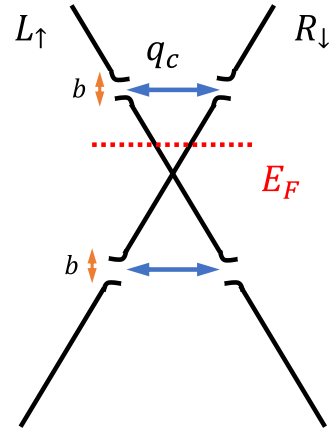

FIG. 4. Spin spiral will not gap out the Dirac cone generically in the absence of disorder. Instead, it will open a gap on the edge of the Brillouin zone at $\pm q_c/2$, where the effective real-space periodicity is defined by the spiral.

the appearance of such an order is the spontaneous arrangement of nuclear spins, here the spin spiral is purely electronic as shown in the Hartree-Fock calculations, giving hope for a more pronounced effect at higher temperatures. Although the spin spiral order breaks the time-reversal symmetry locally, when averaged over the whole period of the spiral the symmetry is still preserved, resulting in a lack of gap opening at the Dirac point of the edge state dispersion. Therefore, we need to also take into account scattering on random nonmagnetic impurities to observe the effect on conductance. To put this on more concrete terms, we use the bosonization technique and compute the deviation from the perfect conductance quantum G_0 below.

A. Fermionic model

We consider the setup for a single layer of QSH insulator WTe_2 as shown in Fig. 3, in the form of a ribbon with open boundary conditions along the y direction. This results in helical edge states (denoted by the red and blue arrows) on the upper and lower boundaries. Based on the results of Hartree-Fock calculations, we further assume the ground state of the QSH insulator has bulk spin-spiral order, denoted by the violet arrows. Such a bulk spin spiral preserves the time-reversal symmetry only when spatially averaged over the period of the spiral along the x direction. As the edge state decay length is very short in WTe_2 [29], we can neglect any coupling between the states located at the opposite boundaries. Focusing thus on states along a single boundary, we can write down the Hamiltonian for helical edge states as

$$H_{\rm hel} = H_{\rm kin} + H_{\rm ee} + H_{\rm m} + H_{\rm imp}, \tag{12}$$

where $H_{\rm kin}$ and $H_{\rm ee}$ are the kinetic energy and electron-electron interactions, respectively. The term $H_{\rm m}$ is the effective magnetic field from the bulk excitonic spin spiral and $H_{\rm imp}$ denotes the nonmagnetic impurities. We further assume that the helical edges are formed by a right-moving mode with spin down ($R_\downarrow$) and a left-moving mode with spin up ($L_\uparrow$). The kinetic energy for the helical edge states reads

$$H_{\rm kin} = -i\hbar v_F \int [dx][R^\dagger_\downarrow(x)\partial_x R_\downarrow(x) - L^\dagger_\uparrow(x)\partial_x L_\uparrow(x)], \tag{13}$$

with the Fermi velocity v_F. When time-reversal symmetry is preserved, the electron-electron interaction $H_{\rm ee} = H^2_{\rm ee} + H^4_{\rm ee}$ contains only forward scattering $H^2_{\rm ee}$ and chiral interaction $H^4_{\rm ee}$:

$$H^2_{\rm ee} = g_2 \int [dx] R^\dagger_\downarrow(x) R_\downarrow(x) L^\dagger_\uparrow(x) L_\uparrow(x), \tag{14a}$$

$$H^4_{\rm ee} = \frac{g_4}{2} \int [dx] \{[R^\dagger_\downarrow(x) R_\downarrow(x)]^2 + [L^\dagger_\uparrow(x) L_\uparrow(x)]^2\}. \tag{14b}$$

The $H_{\rm m}$ captures coupling between the spin density of the edge states and the effective magnetic field induced by the bulk spin spiral order:

$$H_{\rm m} = \int [dx] \sum_{ss'} \psi^\dagger_s(x) [\boldsymbol{B}_{\rm eff}(x) \cdot \boldsymbol{\sigma}_{ss'}] \psi_{s'}(x), \tag{15}$$

where $\boldsymbol{\sigma}$ is a vector of Pauli matrices and $\psi(x) = (L_\uparrow, R_\downarrow)^{\rm T}$. The spatial dependence of the coupling to effective magnetic field $\boldsymbol{B}_{\rm eff}(x)$ can be deduced from the Hartree-Fock mean field and is given by

$$\boldsymbol{B}_{\rm eff}(x) = B_{\rm eff}[\hat{e}_x \cos(q_c x) + \hat{e}_z \sin(q_c x)]. \tag{16}$$

Here $2\pi/q_c$ denotes the period of the bulk spin spiral. In the noninteracting clean limit, i.e., $g_2 = g_4 = 0$ and $H_{\rm imp} = 0$, we can transform Eq. (12) into Fourier space:

$$H'_{\rm hel} = \sum_{k,s,s'} \Big[\psi^\dagger_s(k)(\hbar v_F k \sigma^z_{ss'}) \psi_{s'}(k) + \frac{B_{\rm eff}}{2} \psi^\dagger_s(k+q_c)(\sigma^x_{ss'} - i\sigma^z_{ss'}) \psi_{s'}(k) + {\rm H.c.} \Big]. \tag{17}$$

Note that Eq. (17) couples the right movers and left movers separated by a momentum difference $\pm q_c$. Thus the energy spectrum of the Hamiltonian of Eq. (17) is gapless at $k = 0$, but gaps open for states at momenta $\pm q_c/2$, as shown in Fig. 4. The lack of gap opening at $k = 0$ reflects that $H_{\rm m}$ preserves

the time-reversal symmetry when averaged over real space. This behavior is also in contrast to the previously studied spin spiral state related to the arrangement of nuclear spins. In that case, the gap opens for states separated by $2k_F$, meaning that it occurs on the Fermi surface or is shifted when the chemical potential is changed. However, in the case of a spin spiral state caused by excitonic condensation, the momentum q_c which determines the position of the gap is determined by the electronic band structure and so is not shifting when the charge density is changed via gating. This means that in principle it would be possible to tune the Fermi level into that gap, resulting in a drop in conductance. This could serve as one of the experimental signatures of the excitonic condensation with time-reversal-breaking spin spiral configuration. The exact comparison between the Hartree-Fock results of the previous section and this effective magnetic field is not simple, since the mean-field order parameters in general include many terms that are coupling different orbital degrees of freedom and are in general momentum dependent. However, we can estimate the resultant effect on the spectrum in terms of the gaps that open up in the surface states and conclude that B_{eff} can be on the order of up to a few tens of meV (as high as 50 meV). The exact value however depends on the interaction strength that governs the size of the excitonic order parameter.

Since we are only interested in the impact of the spin spiral on transport properties, we can neglect the forward scattering components of H_{m}, which are the terms proportional to σ_z. Therefore, we can now focus only on the backscattering part, which written in terms of $L_\uparrow(x)$ and $R_\downarrow(x)$ reads

$$H_{\text{m}}^b = \int [dx] \frac{B_{\text{eff}}}{2} \sum_{\delta=\pm} \left[L_\uparrow^\dagger(x) R_\downarrow(x) e^{i q_c^\delta x} + R_\downarrow^\dagger(x) L_\uparrow(x) e^{-i q_c^\delta x} \right], \tag{18}$$

with $q_c^\delta = \pm q_c$. We further model the impurity Hamiltonian as

$$H_{\text{imp}} = \int [dx] V_{\text{imp}}(x) [R_\downarrow^\dagger(x) R_\downarrow(x) + L_\uparrow^\dagger(x) L_\uparrow(x)], \tag{19}$$

where the Gaussian random potential $V_{\text{imp}}(x)$ satisfies $\overline{V_{\text{imp}}(x) V_{\text{imp}}(x')} = M_{\text{imp}} \delta(x - x')$, with $\overline{\cdots}$ denoting the averaging over the random potential. The impurity strength $M_{\text{imp}} = \hbar^2 v_F^2 / (2\pi \lambda_{\text{mfp}})$ here is defined by the mean free path λ_{mfp} of the 2D QSH insulator bulk [40,45,46].

B. Schrieffer-Wolff transformation

We can now derive the combined effect of the random impurities and the spin spiral arising from the excitonic condensate by performing a Schrieffer-Wolff transformation. The full Hamiltonian with the two perturbations included is $H = H_{\text{el}} + \delta V$, where $\delta V = H_{\text{imp}} + H_{\text{m}}$. This can be transformed into momentum space using

$$R_\downarrow(x) = \frac{1}{\sqrt{L}} \sum_k e^{ikx} R_\downarrow(k), \quad L_\uparrow(x) = \frac{1}{\sqrt{L}} \sum_k e^{ikx} L_\uparrow(k), \tag{20}$$

such that we have kinetic energy diagonal in momentum space

$$H_{\text{kin}} = \sum_k \hbar v_F k [R_\downarrow^\dagger(k) R_\downarrow(k) - L_\uparrow^\dagger(k) L_\uparrow(k)]. \tag{21}$$

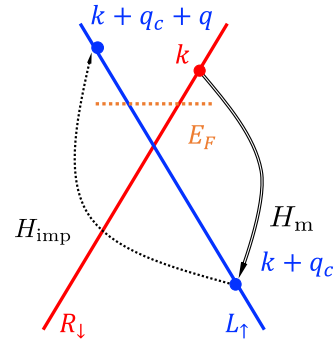

FIG. 5. Spin spiral assisted backscattering on nonmagnetic impurities. The initial right moving state with momentum k is first scattered by the spin spiral to a left mover with momentum $k + q_c$ and then forward scattered by an impurity to a left moving state with momentum $k + q_c + q$. At low temperatures, the leading scattering processes will have the initial and final state in the vicinity of the Fermi energy E_F.

The impurity contributes arbitrary momentum shift in the forward scattering process

$$H_{\text{imp}} = \sum_{k,q} \frac{V_{\text{imp}}(q)}{L} (R_\downarrow^\dagger(k+q) R_\downarrow(k) + L_\uparrow^\dagger(k+q) L_\uparrow(k)) \tag{22}$$

and the coupling to the spin spiral reads

$$H_{\text{m}} = \frac{B_{\text{eff}}}{2L} \sum_{k,\delta} \left[L_\uparrow^\dagger\left(k + q_c^\delta\right) R_\downarrow(k) + R_\downarrow^\dagger\left(k + q_c^\delta\right) L_\uparrow(k) \right], \tag{23}$$

which changes a right to a left mover and vice versa together with a momentum shift $\pm q_c$ determined by the period of the spin spiral. The forward scattering from H_{imp} on its own does not change the conductivity and, at low temperatures, the initial and final states in backscattering process should come from the vicinity of the Fermi level. Therefore, neither H_{imp} nor H_{m} in 1D can affect conductivity on their own. However, a combined spin spiral and impurity scattering can lead to the relaxation of the current through a second-order process, an example of which is illustrated in Fig. 5. This is a second-order effect, where the H_{m} first backscatters a state with momentum k to $k + q_c$ $(k - q_c)$ and then H_{imp} brings the state back to the region near the Fermi level through the forward scattering with the disorder potential. We see that the scattering with a combination of the spin spiral and nonmagnetic disorder can be viewed as the scattering with an effective magnetic disorder, though the former pattern still respects time-reversal symmetry on average. We term this kind of the current relaxation mechanism as the spin-spiral assisted backscattering.

The intuitive picture of spin-spiral assisted backscattering presented above can be captured by the Schrieffer-Wolff transformation. For simplicity, we first consider the noninteracting case where $H_{\text{el}} = H_{\text{kin}}$:

$$H' = e^S H e^{-S} = H_{\text{kin}} + \delta V + [S, H_{\text{kin}}] + [S, \delta V] + \tfrac{1}{2}[S, [S, H_{\text{kin}}]] + \tfrac{1}{2}[S, [S, \delta V]] + \cdots. \tag{24}$$

We can now choose S such that the transformed Hamiltonian H' does not depend on perturbation couplings to linear order by fulfilling the condition $\delta V + [S, H_{\rm kin}] = 0$. Since $H_{\rm kin}$ is diagonal in momentum space, we can write down the matrix element $S_{\alpha\beta}$ between the two eigenstates α and β of $H_{\rm kin}$:

$$S_{\alpha\beta} = \frac{\delta V_{\alpha\beta}}{E_\alpha - E_\beta}. \tag{25}$$

Substituting this back into H', we obtain

$$H'_{\alpha\beta} = E_\alpha \delta_{\alpha\beta} + \frac{1}{2}\sum_\gamma \left(\frac{\delta V_{\alpha\gamma}\delta V_{\gamma\beta}}{E_\alpha - E_\gamma} + \frac{\delta V_{\alpha\gamma}\delta V_{\gamma\beta}}{E_\gamma - E_\beta}\right) + O(\delta V^3). \tag{26}$$

We can now consider how the original Hamiltonian acts within the subspace of the three states presented in Fig. 5. In the basis of $\Psi = [R_\downarrow(k), L_\uparrow(k+q_c), L_\uparrow(k+q_c+q)]/L$, we have

$$h(k,q) = \Psi^\dagger \begin{pmatrix} \hbar v_F k & 0 & B_{\rm eff}/2 \\ 0 & -\hbar v_F(k+q_c+q) & V_{\rm imp} \\ B_{\rm eff}/2 & V_{\rm imp} & -\hbar v_F(k+q_c) \end{pmatrix} \Psi. \tag{27}$$

Using these matrix elements in combination with Eq. (26), we find

$$\Delta h(k,q) = \frac{B_{\rm eff}}{4}\left(\frac{V_{\rm imp}(q)}{\hbar v_F(2k+q_c)} - \frac{V_{\rm imp}(q)}{\hbar v_F q}\right). \tag{28}$$

Now we need to take into account the conservation of energy in the whole scattering process. The majority of the contribution in the low temperature limit is given by the states with an identical energy for the initial and final states around the Fermi level: with initial $k \sim k_F$, these energies are $\hbar v_F k_F$ and $-\hbar v_F(k_F + q_c - q)$, leading to $q = -2k_F - q_c + k'$. In such limit, we have

$$\Delta h(k') \approx \frac{B_{\rm eff}}{2}\frac{V_{\rm imp}(-2k_F - q_c + k')}{\hbar v_F(2k_F + q_c)}. \tag{29}$$

A similar procedure follows for the other possible scattering processes and in the end the effective backscattering reads

$$H_{\rm eff} = \sum_{k,k',\delta}[V^\delta(k')L^\dagger_\uparrow(k - 2k_F + k')R_\downarrow(k) + \text{H.c.}], \tag{30}$$

where $V^\pm(k') = B_{\rm eff}V_{\rm imp}(-2k_F \mp q_c + k')/[2L^2\hbar v_F(2k_F \pm q_c)]$. The above results hold even in the interacting case, provided that $g_2 = g_4$ [46]. While Eq. (30) looks very much similar to Eq. (D5) in Ref. [46], the physical interpretation is quite different. In Ref. [46], the spin spiral arises from the RKKY coupling of nuclear spins, whereas in our case it comes from the time-reversal-breaking excitonic condensate. The nuclear spin spiral period is thus directly related to k_F and changes with chemical potential, while the excitonic spiral is determined by the momentum space separation between the electron and hole pockets in the band structure and is fixed.

Equation (30) can be transformed into real space by the inverse Fourier transformation after which the Hamiltonian reads

$$H_{\rm eff} = \int [dx][\xi(x)L^\dagger_\uparrow(x)R_\downarrow(x) + \xi^*(x)R^\dagger_\downarrow(x)L_\uparrow(x)], \tag{31}$$

with

$$\xi(x) = B_{\rm eff}\frac{2k_F\cos(q_c x) + iq_c\sin(q_c x)}{\hbar v_F\left(4k_F^2 - q_c^2\right)}V_{\rm imp}(x). \tag{32}$$

The correlation function of $\xi(x)$ averaged over the disorder realizations can be deduced from the correlation of $V_{\rm imp}(x)$ to be

$$\overline{\xi(x)\xi^*(x')} = M_{\rm ss}\delta(x - x'), \tag{33}$$

with

$$M_{\rm ss} = M_{\rm imp}\frac{B_{\rm eff}^2\left(4k_F^2 + q_c^2\right)}{2\hbar^2 v_F^2\left(4k_F^2 - q_c^2\right)^2}, \tag{34}$$

where we used the fact that $\overline{\cos^2(q_c x)} = \overline{\sin^2(q_c x)} = 1/2$.

C. Bosonization result for transport properties

With the effective spin spiral assisted backscattering Hamiltonian derived, we can determine its impact on transport properties using bosonization, which is especially well suited for studying two-terminal transport in a disordered 1D quantum system [40,45,46,51,60,76–80]. The chiral component in Eq. (12) can be expressed in terms of the bosonic field (θ, ϕ) [40,45,46,51,60,79,80]:

$$R_\downarrow(x) = \frac{U_R}{\sqrt{2\pi\alpha}}e^{ik_F x}e^{i[-\phi(x)+\theta(x)]},$$
$$L_\uparrow(x) = \frac{U_L}{\sqrt{2\pi\alpha}}e^{-ik_F x}e^{i[\phi(x)+\theta(x)]}, \tag{35}$$

where $U_{R/L}$ is the Klein factor and $\alpha = \hbar v_F/\Delta_b$ is the short-distance cutoff, which is associated with the high-energy cutoff set by the bulk gap Δ_b. With the above definitions, the helical Hamiltonian without $H_{\rm m}$ can be bosonized in a standard way as

$$H_{\rm kin} + H_{\rm ee} = \frac{\hbar u}{2\pi}\int [dx]\left[\frac{1}{K}(\partial_x\phi)^2 + K(\partial_x\theta)^2\right], \tag{36}$$

where the velocity u and the interaction parameter K are given by

$$u = \left[\left(v_F + \frac{g_4}{h}\right)^2 - \left(\frac{g_2}{h}\right)^2\right]^{1/2},$$
$$K \equiv \left(\frac{hv_F + g_4 - g_2}{hv_F + g_4 + g_2}\right)^{1/2}. \tag{37}$$

To find the bosonized form of the effective backscattering Hamiltonian $H_{\rm eff}$ averaged over disorder, we utilize the replica method and, similarly to Ref. [46], we obtain the effective backscattering action:

$$\frac{\delta S_{\rm ss}}{\hbar} = -\frac{M_{\rm ss}}{(2\pi\hbar a)^2}\int_{u|\tau-\tau'|>a} dx\, d\tau\, d\tau' \times \cos[2\phi(x,\tau) - 2\phi(x,\tau')]. \tag{38}$$

In the absence of disorder, so long as the Fermi level is not placed within the gap (see in Fig. 4), the Hamiltonian Eq. (12)

is similar to the edge of the time-reversal invariant QSH insulator, which has a quantized zero-temperature conductance $G = G_0 \equiv e^2/h$ (equivalently, resistance $R_0 = h/e^2$) per edge. Following the results of Ref. [40], we find the increase of the resistivity R_{ss} due to the combination of bulk spin spiral and nonmagnetic disorder depends on the relative magnitude of three possible physical cutoffs. These cutoffs are the edge length L, the thermal length $\lambda_T \equiv \hbar u/(k_B T)$, and the localization length ξ_{ss}. We define the dimensionless coupling constant,

$$D_{ss} \equiv \frac{2aM_{ss}}{(\pi \hbar^2 u^2)}, \tag{39}$$

and $u = v_F/K$. If the edge length is the shortest among all these scales, $L < \lambda_T,\ \xi_{ss}$, the correction to edge resistance, is

$$\delta R_{ss}(L) \propto R_0 \frac{M_{ss} L}{\hbar^2 v_F^2} L^{2-2K} = R_0 \frac{\pi D_{ss}}{2K^2} \left(\frac{L}{a}\right)^{3-2K}. \tag{40}$$

Secondly, in the limit of high temperatures where $\lambda_T < L,\ \xi_{ss}$, we get

$$\delta R_{ss}(T) \propto R_0 \frac{M_{ss} L}{\hbar^2 v_F^2} \lambda_T^{2-2K} = R_0 \frac{\pi D_{ss} L}{2K^2 a} \left(\frac{K k_B T}{\Delta}\right)^{2K-2}. \tag{41}$$

Finally, if $\xi_{ss} < L, \lambda_T$, the RG flow reaches the strong coupling regime, so the edge states are gapped, displaying a thermally activated resistance:

$$\delta R_{ss}(T) \propto R_0 \frac{\pi D_{ss} L}{2K^2 a} e^{\Delta_{ss}/(k_B T)}, \tag{42}$$

with the gap $\Delta_{ss} = \Delta(2KD_{ss})^{1/(3-2K)}$.

The scaling with respect to the length of the edge and the temperature of the sample can in principle be measured experimentally and be used to obtain the K parameter of the edge state. However, currently available data is insufficient to arrive at such an estimate.

IV. CONCLUSION

In conclusion, we provided a mechanism for the breakdown of the perfect conductance quantization in WTe_2 due to the formation of a time-reversal-breaking excitonic condensate with a bulk spin spiral order. Through Hartree-Fock calculations we showed the difference between the time-reversal-preserving and -breaking excitonic condensates that can form in WTe_2 depending on the circumstances. Based on the mean-field results, we performed quantum transport calculations for a finite width ribbon with disorder based on a lattice model. We demonstrated that, while the time-reversal-preserving excitonic insulator is topological and thus exhibits robust conductance quantization of edge state transport, the time-reversal-breaking condensate deviates from e^2/h per edge conductance in the presence of nonmagnetic static disorder. Our results are in good agreement with the experimentally observed edge-length scaling of resistance with results close to quantized below 100 nm with the deviation increasing substantially for longer edges.

To provide some additional intuition for the mechanism behind the breakdown, we then supplemented these simulations by analytical edge transport calculations in the Luttinger liquid picture. Similarly to the previous work on the effect of RKKY nuclear spin spiral on helical edge states [46], we used the Schrieffer-Wolff transformation to capture the effective spin-spiral assisted backscattering from the nonmagnetic impurities. This provides a qualitative understanding of the effective backscattering in disordered excitonic condensate with spin spiral order. Finally, by using bosonization, we determine the effect of this backscattering process on the transport properties of the system, determining the scaling dependence of resistance on length, temperature, and interaction strength.

Our work thus provides a new mechanism which possibly contributes to the lack of perfect quantization in WTe_2 and paves the way for bridging the bulk and edge transport theory. It also encourages further experimental investigation to verify the presence of the spin spiral excitonic condensate. For example, application of external magnetic field in the spin spiral phase should lead to the appearance of a charge density wave state that could be detected using scanning tunneling microscopy (STM). Moreover, since the direction of the spin spiral is directly determined by the crystalline axes, its impact on the edge state properties would be directly dependent on the edge orientation with respect to the spin spiral. The spatial periodicity of the spin spiral may also contribute to the modulation of the edge states, which could be observed using STM in quasiparticle interference patterns [81]. These and other potential experiments are necessary to verify the true nature of the ground state of WTe_2, providing exciting new research directions. Our results can also be generalized to transport in many other quantum physics systems with topologically protected edge states such as twisted multilayer graphene [82].

ACKNOWLEDGMENTS

This work was supported as part of the Center for Novel Pathways to Quantum Coherence in Materials, an Energy Frontier Research Center funded by the U.S. Department of Energy, Office of Science, Basic Energy Sciences (Y.-Q.W. and J.E.M.). M.P. was supported by the Quantum Science Center (QSC), a National Quantum Information Science Research Center of the U.S. Department of Energy (DOE). M.P. received additional fellowship support from the Emergent Phenomena in Quantum Systems program of the Gordon and Betty Moore Foundation.

APPENDIX: ADDITIONAL DETAILS OF MEAN-FIELD CALCULATION AND TRANSPORT SIMULATION

We perform the Hartree-Fock calculations using the lattice version of the model in Eq. (1). Before any band folding or inclusion of interaction effects takes place, the model consists of four bands, corresponding to hybridization of two orbital and two spin degrees of freedom. With the parameter set listed below Eq. (1) the system is in semimetallic phase and the corresponding band structure in the region of interest inside the Brillouin zone is presented in Fig. 6(a). The horizontal dashed line indicates the position of the Fermi level, which demonstrates the presence of both electron and hole pockets, with the electron pocket centered around points $\pm q_c$ along the $\Gamma - \tilde{X}$ direction of the original Brillouin zone. As we are looking for mean-field order parameters that couple states

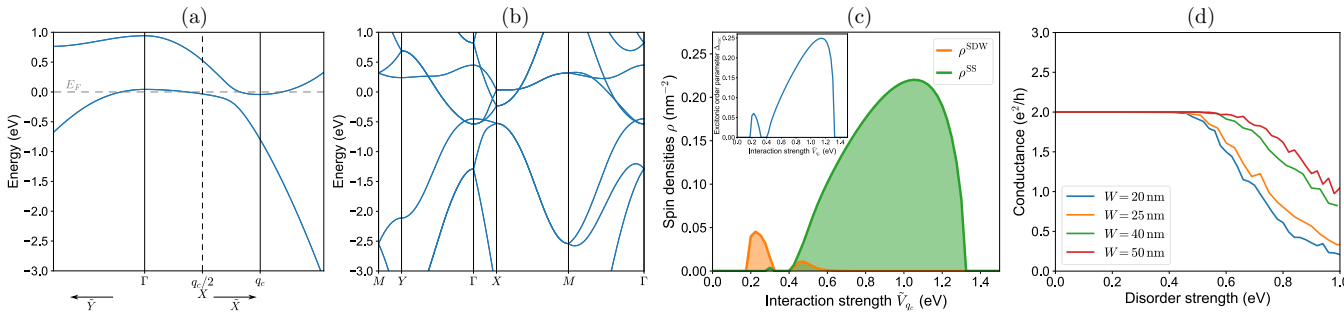

FIG. 6. (a) Band structure of Hamiltonian (1) before folding. The position of the electron pocket is indicated by the line at q_c and the folding is performed across the $q_c/2$ line. (b) Band structure after folding, with X point being the $q_c/2$ point of the original band structure. (c) The phase diagram of the excitonic phases with respect to the interaction strength, separated into spin density wave and spin spiral states characterized by densities ρ^{SDW} and ρ^{SS} given by Eq. (9). The inset shows overall excitonic condensate order parameter Δ_{exc}. (d) Transport simulation for ribbons of 200 nm length and increasing width in the time-reversal invariant case. Results are averaged over 100 disorder realizations.

separated by momentum q_c, it is convenient to perform the calculations using the scheme with bands folded across the vertical dashed line that crosses the $q_c/2$ point as indicated in the figure. The $q_c/2$ point then becomes the X point of the folded Brillouin zone. The band structure after folding, which is the starting point for the Hartree-Fock calculation, is shown in Fig. 6(b). We now clearly see the overlap of the electron and hole pockets, which after folding both end up at the Γ point. With such a setup we perform the self-consistent calculation using the prescription given in the main text.

We characterize the results of the self-consistent calculation using quantities given by Eqs. (7) and (9), which show the presence of the excitonic condensate and its spin character, respectively. According to our results, when time-reversal symmetry is not enforced, the calculation will always generate time-reversal-breaking terms that lead to either spin density wave or spin spiral state whenever the excitonic condensate is formed. The phase diagram depends on the strength of interaction, characterized by $\tilde{V}_{q_c}$, and is shown in Fig. 6(c). It consists of two regions, separated by a small section which does not host the excitonic phase. Of the two regions the much more pronounced one describes the spin spiral phase, which is the focus of this work. It spans over a broad range of interaction strengths, suggesting its potential stability. On the other hand, the spin density wave phase occupies only a small region of interaction strength space and requires substantially weakened Coulomb interaction. In the inset, we demonstrate that both of these phases are excitonic condensates, which are captured through the order parameter Δ_{exc}. We do not observe any excitonic phases outside of the regions in which either spin spiral or spin density wave states are present. As the starting point for our calculations is a gapless semimetallic phase, the exciton condensation occurs as long as there is energy gain coming from forming the electron-hole pairs. This is in contrast to a more common scenario in which excitons are formed out of electron and hole states at the same momentum, separated by the material band gap. In that case, for the condensation to occur the exciton binding energy has to be larger than the band gap. Nevertheless, we can estimate the energy gain of the exciton condensate with respect to the semimetallic phase to be on the order of 110 meV, with the exact value dependent on the strength of interaction. While we have multiple different order parameters, we can also estimate the binding energy of excitons by the largest value of the excitonic order parameter. In the case of spin spiral state chosen for the quantum transport simulation, this value is about 36 meV. Both of these energy estimates suggest the relative stability of the excitonic condensate in this system. When time-reversal symmetry is enforced, a single excitonic dome is observed. The phase diagram for that scenario is presented in the Supplemental Material of Ref. [65].

We also present additional transport results in the time-reversal-preserving case in Fig. 6(d). These results demonstrate that when the time-reversal symmetric excitonic condensate is present in the system, as the width of the ribbon gets increased, so does the disorder strength for which the conductance quantization breaks down. This indicates that the backscattering necessary for this breakdown does not occur within the same edge, but requires coupling between the opposite edges. This could be compared to a percolationlike transition, which requires sufficient disorder strength for a conducting path to connect the opposite edges of the ribbon. On the other hand, in the time-reversal-breaking spin spiral state, the backscattering occurs within the same edge, so increasing the ribbon width does not change its transport characteristics.

[1] C. L. Kane and E. J. Mele, Quantum spin Hall effect in graphene, Phys. Rev. Lett. **95**, 226801 (2005).

[2] C. L. Kane and E. J. Mele, Z_2 topological order and the quantum spin Hall effect, Phys. Rev. Lett. **95**, 146802 (2005).

[3] B. A. Bernevig and S.-C. Zhang, Quantum spin Hall effect, Phys. Rev. Lett. **96**, 106802 (2006).

[4] M. Z. Hasan and C. L. Kane, Colloquium: Topological insulators, Rev. Mod. Phys. **82**, 3045 (2010).

[5] X.-L. Qi and S.-C. Zhang, Topological insulators and superconductors, Rev. Mod. Phys. **83**, 1057 (2011).

[6] J. Alicea, New directions in the pursuit of Majorana fermions in solid state systems, Rep. Prog. Phys. **75**, 076501 (2012).

[7] Y. Ren, Z. Qiao, and Q. Niu, Topological phases in two-dimensional materials: a review, Rep. Prog. Phys. **79**, 066501 (2016).

[8] D. Culcer, A. C. Keser, Y. Li, and G. Tkachov, Transport in two-dimensional topological materials: recent developments in experiment and theory, 2D Mater. **7**, 022007 (2020).

[9] J. I. Väyrynen, D. I. Pikulin, and J. Alicea, Noise-induced backscattering in a quantum spin Hall edge, Phys. Rev. Lett. **121**, 106601 (2018).

[10] M. Konig, S. Wiedmann, C. Brune, A. Roth, H. Buhmann, L. W. Molenkamp, X.-L. Qi, and S.-C. Zhang, Quantum spin Hall insulator state in HgTe quantum wells, Science **318**, 766 (2007).

[11] A. Roth, C. Brüne, H. Buhmann, L. W. Molenkamp, J. Maciejko, X.-L. Qi, and S.-C. Zhang, Nonlocal transport in the quantum spin Hall state, Science **325**, 294 (2009).

[12] I. Knez, R.-R. Du, and G. Sullivan, Evidence for helical edge modes in inverted InAs/GaSb quantum wells, Phys. Rev. Lett. **107**, 136603 (2011).

[13] E. M. Spanton, K. C. Nowack, L. Du, G. Sullivan, R.-R. Du, and K. A. Moler, Images of edge current in InAs/GaSb quantum wells, Phys. Rev. Lett. **113**, 026804 (2014).

[14] V. S. Pribiag, A. J. A. Beukman, F. Qu, M. C. Cassidy, C. Charpentier, W. Wegscheider, and L. P. Kouwenhoven, Edge-mode superconductivity in a two-dimensional topological insulator, Nat. Nanotechnol. **10**, 593 (2015).

[15] L. Du, I. Knez, G. Sullivan, and R.-R. Du, Robust helical edge transport in gated InAs/GaSb bilayers, Phys. Rev. Lett. **114**, 096802 (2015).

[16] T. Li, P. Wang, H. Fu, L. Du, K. A. Schreiber, X. Mu, X. Liu, G. Sullivan, G. A. Csáthy, X. Lin, and R.-R. Du, Observation of a helical Luttinger liquid in InAs/GaSb quantum spin Hall edges, Phys. Rev. Lett. **115**, 136804 (2015).

[17] L. Du, T. Li, W. Lou, X. Wu, X. Liu, Z. Han, C. Zhang, G. Sullivan, A. Ikhlassi, K. Chang, and R.-R. Du, Tuning edge states in strained-layer InAs/GaInSb quantum spin Hall insulators, Phys. Rev. Lett. **119**, 056803 (2017).

[18] L. Du, X. Li, W. Lou, G. Sullivan, K. Chang, J. Kono, and R.-R. Du, Evidence for a topological excitonic insulator in InAs/GaSb bilayers, Nat. Commun. **8**, 1971 (2017).

[19] K. Bendias, S. Shamim, O. Herrmann, A. Budewitz, P. Shekhar, P. Leubner, J. Kleinlein, E. Bocquillon, H. Buhmann, and L. W. Molenkamp, High mobility HgTe microstructures for quantum spin Hall studies, Nano Lett. **18**, 4831 (2018).

[20] L. Lunczer, P. Leubner, M. Endres, V. L. Müller, C. Brüne, H. Buhmann, and L. W. Molenkamp, Approaching quantization in macroscopic quantum spin Hall devices through gate training, Phys. Rev. Lett. **123**, 047701 (2019).

[21] D. Xiao, C.-X. Liu, N. Samarth, and L.-H. Hu, Anomalous quantum oscillations of interacting electron-hole gases in inverted type-II InAs/GaSb quantum wells, Phys. Rev. Lett. **122**, 186802 (2019).

[22] Z. Han, T. Li, L. Zhang, G. Sullivan, and R.-R. Du, Anomalous conductance oscillations in the hybridization gap of InAs/GaSb quantum wells, Phys. Rev. Lett. **123**, 126803 (2019).

[23] S. U. Piatrusha, E. S. Tikhonov, Z. D. Kvon, N. N. Mikhailov, S. A. Dvoretsky, and V. S. Khrapai, Topological protection brought to light by the time-reversal symmetry breaking, Phys. Rev. Lett. **123**, 056801 (2019).

[24] J. Strunz, J. Wiedenmann, C. Fleckenstein, L. Lunczer, W. Beugeling, V. L. Müller, P. Shekhar, N. T. Ziani, S. Shamim, J. Kleinlein *et al.*, Interacting topological edge channels, Nat. Phys. **16**, 83 (2020).

[25] S. Shamim, W. Beugeling, J. Böttcher, P. Shekhar, A. Budewitz, P. Leubner, L. Lunczer, E. M. Hankiewicz, H. Buhmann, and L. W. Molenkamp, Emergent quantum Hall effects below 50 mT in a two-dimensional topological insulator, Sci. Adv. **6**, eaba4625 (2020).

[26] M. C. Dartiailh, S. Hartinger, A. Gourmelon, K. Bendias, H. Bartolomei, H. Kamata, J.-M. Berroir, G. Fève, B. Plaçais, L. Lunczer, R. Schlereth, H. Buhmann, L. W. Molenkamp, and E. Bocquillon, Dynamical separation of bulk and edge transport in HgTe-based 2D topological insulators, Phys. Rev. Lett. **124**, 076802 (2020).

[27] S. Shamim, W. Beugeling, P. Shekhar, K. Bendias, L. Lunczer, J. Kleinlein, H. Buhmann, and L. W. Molenkamp, Quantized spin Hall conductance in a magnetically doped two dimensional topological insulator, Nat. Commun. **12**, 3193 (2021).

[28] B. A. Bernevig, T. L. Hughes, and S.-C. Zhang, Quantum spin hall effect and topological phase transition in hgte quantum wells, Science **314**, 1757 (2006).

[29] M. Bieniek, J. I. Väyrynen, G. Li, T. Neupert, and R. Thomale, Theory of glide symmetry protected helical edge states in WTe_2 monolayer, Phys. Rev. B **107**, 195105 (2023).

[30] X. Qian, J. Liu, L. Fu, and J. Li, Quantum spin Hall effect in two-dimensional transition metal dichalcogenides, Science **346**, 1344 (2014).

[31] Z. Fei, T. Palomaki, S. Wu, W. Zhao, X. Cai, B. Sun, P. Nguyen, J. Finney, X. Xu, and D. H. Cobden, Edge conduction in monolayer WTe_2, Nat. Phys. **13**, 677 (2017).

[32] S. Tang, C. Zhang, D. Wong, Z. Pedramrazi, H.-Z. Tsai, C. Jia, B. Moritz, M. Claassen, H. Ryu, S. Kahn *et al.*, Quantum spin Hall state in monolayer 1T′-WTe_2, Nat. Phys. **13**, 683 (2017).

[33] S. Wu, V. Fatemi, Q. D. Gibson, K. Watanabe, T. Taniguchi, R. J. Cava, and P. Jarillo-Herrero, Observation of the quantum spin Hall effect up to 100 kelvin in a monolayer crystal, Science **359**, 76 (2018).

[34] Z. Li, Y. Song, and S. Tang, Quantum spin Hall state in monolayer 1T′-TMDCs, J. Phys.: Condens. Matter **32**, 333001 (2020).

[35] Z.-Y. Jia, Y.-H. Song, X.-B. Li, K. Ran, P. Lu, H.-J. Zheng, X.-Y. Zhu, Z.-Q. Shi, J. Sun, J. Wen, D. Xing, and S.-C. Li, Direct visualization of a two-dimensional topological insulator in the single-layer 1T′-WTe_2, Phys. Rev. B **96**, 041108(R) (2017).

[36] L. Peng, Y. Yuan, G. Li, X. Yang, J.-J. Xian, C.-J. Yi, Y.-G. Shi, and Y.-S. Fu, Observation of topological states residing at step edges of WTe_2, Nat. Commun. **8**, 659 (2017).

[37] G. M. Gusev, Z. D. Kvon, E. B. Olshanetsky, A. D. Levin, Y. Krupko, J. C. Portal, N. N. Mikhailov, and S. A. Dvoretsky, Temperature dependence of the resistance of a two-dimensional topological insulator in a HgTe quantum well, Phys. Rev. B **89**, 125305 (2014).

[38] I. Knez, C. T. Rettner, S.-H. Yang, S. S. P. Parkin, L. Du, R.-R. Du, and G. Sullivan, Observation of edge transport in the disordered regime of topologically insulating InAs/GaSb quantum wells, Phys. Rev. Lett. **112**, 026602 (2014).

[39] F. Nichele, H. J. Suominen, M. Kjaergaard, C. M. Marcus, E. Sajadi, J. A. Folk, F. Qu, A. J. A. Beukman, F. K. deVries, J. V. Veen, S. Nadj-Perge, L. P. Kouwenhoven, B.-M. Nguyen, A. A. Kiselev, W. Yi, M. Sokolich, M. J. Manfra, E. M. Spanton, and K. A. Moler, Edge transport in the trivial phase of InAs/GaSb, New J. Phys. **18**, 083005 (2016).

[40] C.-H. Hsu, P. Stano, J. Klinovaja, and D. Loss, Helical liquids in semiconductors, Semicond. Sci. Technol. **36**, 123003 (2021).

[41] T. L. Schmidt, S. Rachel, F. von Oppen, and L. I. Glazman, Inelastic electron backscattering in a generic helical edge channel, Phys. Rev. Lett. **108**, 156402 (2012).

[42] N. Lezmy, Y. Oreg, and M. Berkooz, Single and multiparticle scattering in helical liquid with an impurity, Phys. Rev. B **85**, 235304 (2012).

[43] J. I. Väyrynen, M. Goldstein, Y. Gefen, and L. I. Glazman, Resistance of helical edges formed in a semiconductor heterostructure, Phys. Rev. B **90**, 115309 (2014).

[44] J. I. Väyrynen, M. Goldstein, and L. I. Glazman, Helical edge resistance introduced by charge puddles, Phys. Rev. Lett. **110**, 216402 (2013).

[45] C.-H. Hsu, P. Stano, J. Klinovaja, and D. Loss, Nuclear-spin-induced localization of edge states in two-dimensional topological insulators, Phys. Rev. B **96**, 081405(R) (2017).

[46] C.-H. Hsu, P. Stano, J. Klinovaja, and D. Loss, Effects of nuclear spins on the transport properties of the edge of two-dimensional topological insulators, Phys. Rev. B **97**, 125432 (2018).

[47] C. Wu, B. A. Bernevig, and S.-C. Zhang, Helical liquid and the edge of quantum spin Hall systems, Phys. Rev. Lett. **96**, 106401 (2006).

[48] C. Xu and J. E. Moore, Stability of the quantum spin Hall effect: Effects of interactions, disorder, and Z_2 topology, Phys. Rev. B **73**, 045322 (2006).

[49] A. Ström, H. Johannesson, and G. I. Japaridze, Edge dynamics in a quantum spin Hall state: Effects from Rashba spin-orbit interaction, Phys. Rev. Lett. **104**, 256804 (2010).

[50] F. Geissler, F. Crépin, and B. Trauzettel, Random Rashba spin-orbit coupling at the quantum spin Hall edge, Phys. Rev. B **89**, 235136 (2014).

[51] N. Kainaris, I. V. Gornyi, S. T. Carr, and A. D. Mirlin, Conductivity of a generic helical liquid, Phys. Rev. B **90**, 075118 (2014).

[52] H.-Y. Xie, H. Li, Y.-Z. Chou, and M. S. Foster, Topological protection from random Rashba spin-orbit backscattering: Ballistic transport in a helical Luttinger liquid, Phys. Rev. Lett. **116**, 086603 (2016).

[53] M. Kharitonov, F. Geissler, and B. Trauzettel, Backscattering in a helical liquid induced by Rashba spin-orbit coupling and electron interactions: Locality, symmetry, and cutoff aspects, Phys. Rev. B **96**, 155134 (2017).

[54] A. Del Maestro, T. Hyart, and B. Rosenow, Backscattering between helical edge states via dynamic nuclear polarization, Phys. Rev. B **87**, 165440 (2013).

[55] F. Crépin, J. C. Budich, F. Dolcini, P. Recher, and B. Trauzettel, Renormalization group approach for the scattering off a single Rashba impurity in a helical liquid, Phys. Rev. B **86**, 121106(R) (2012).

[56] J. C. Budich, F. Dolcini, P. Recher, and B. Trauzettel, Phonon-induced backscattering in helical edge states, Phys. Rev. Lett. **108**, 086602 (2012).

[57] S. Groenendijk, G. Dolcetto, and T. L. Schmidt, Fundamental limits to helical edge conductivity due to spin-phonon scattering, Phys. Rev. B **97**, 241406(R) (2018).

[58] D. I. Pikulin and T. Hyart, Interplay of exciton condensation and the quantum spin Hall effect in InAs/GaSb bilayers, Phys. Rev. Lett. **112**, 176403 (2014).

[59] A. Blason and M. Fabrizio, Exciton topology and condensation in a model quantum spin Hall insulator, Phys. Rev. B **102**, 035146 (2020).

[60] Y. H. Kwan, T. Devakul, S. L. Sondhi, and S. A. Parameswaran, Theory of competing excitonic orders in insulating WTe_2 monolayers, Phys. Rev. B **104**, 125133 (2021).

[61] A. Amaricci, G. Mazza, M. Capone, and M. Fabrizio, Exciton condensation in strongly correlated quantum spin Hall insulators, Phys. Rev. B **107**, 115117 (2023).

[62] V. Fatemi, S. Wu, Y. Cao, L. Bretheau, Q. D. Gibson, K. Watanabe, T. Taniguchi, R. J. Cava, and P. Jarillo-Herrero, Electrically tunable low-density superconductivity in a monolayer topological insulator, Science **362**, 926 (2018).

[63] D. Varsano, M. Palummo, E. Molinari, and M. Rontani, A monolayer transition-metal dichalcogenide as a topological excitonic insulator, Nat. Nanotechnol. **15**, 367 (2020).

[64] B. Sun, W. Zhao, T. Palomaki, Z. Fei, E. Runburg, P. Malinowski, X. Huang, J. Cenker, Y.-T. Cui, J.-H. Chu *et al.*, Evidence for equilibrium exciton condensation in monolayer WTe_2, Nat. Phys. **18**, 94 (2022).

[65] Y. Jia, P. Wang, C.-L. Chiu, Z. Song, G. Yu, B. Jäck, S. Lei, S. Klemenz, F. A. Cevallos, M. Onyszczak, N. Fishchenko, X. Liu, G. Farahi, F. Xie, Y. Xu, K. Watanabe, T. Taniguchi, B. A. Bernevig, R. J. Cava, L. M. Schoop *et al.*, Evidence for a monolayer excitonic insulator, Nat. Phys. **18**, 87 (2022).

[66] T. Paul, V. F. Becerra, and T. Hyart, Interplay of quantum spin Hall effect and spontaneous time-reversal symmetry breaking in electron-hole bilayers. I. Transport properties, Phys. Rev. B **106**, 235420 (2022).

[67] T. Paul, V. F. Becerra, and T. Hyart, Interplay of quantum spin Hall effect and spontaneous time-reversal symmetry breaking in electron-hole bilayers. II. Zero-field topological superconductivity, Phys. Rev. B **106**, 235421 (2022).

[68] J. Jia, E. Marcellina, A. Das, M. S. Lodge, B. Wang, D.-Q. Ho, R. Biswas, T. A. Pham, W. Tao, C.-Y. Huang, H. Lin, A. Bansil, S. Mukherjee, and B. Weber, Tuning the many-body interactions in a helical Luttinger liquid, Nat. Commun. **13**, 6046 (2022).

[69] R. E. Throckmorton and O. Vafek, Fermions on bilayer graphene: Symmetry breaking for $B = 0$ and $\nu = 0$, Phys. Rev. B **86**, 115447 (2012).

[70] Z. A. H. Goodwin, V. Vitale, F. Corsetti, D. K. Efetov, A. A. Mostofi, and J. Lischner, Critical role of device geometry for the phase diagram of twisted bilayer graphene, Phys. Rev. B **101**, 165110 (2020).

[71] Z. A. H. Goodwin, V. Vitale, X. Liang, A. A. Mostofi, and J. Lischner, Hartree theory calculations of quasiparticle properties in twisted bilayer graphene, Electron. Struct. **2**, 034001 (2020).

[72] K. Kolar, Y. Zhang, S. Nadj-Perge, F. von Oppen, and C. Lewandowski, The electrostatic fate of N-layer moiré graphene, arXiv:2307.07531.

[73] N. Bultinck, E. Khalaf, S. Liu, S. Chatterjee, A. Vishwanath, and M. P. Zaletel, Ground state and hidden symmetry of

magic-angle graphene at even integer filling, Phys. Rev. X **10**, 031034 (2020).

[74] T. Soejima, D. E. Parker, N. Bultinck, J. Hauschild, and M. P. Zaletel, Efficient simulation of moiré materials using the density matrix renormalization group, Phys. Rev. B **102**, 205111 (2020).

[75] C. W. Groth, M. Wimmer, A. R. Akhmerov, and X. Waintal, Kwant: a software package for quantum transport, New J. Phys. **16**, 063065 (2014).

[76] I. Safi and H. J. Schulz, Transport in an inhomogeneous interacting one-dimensional system, Phys. Rev. B **52**, R17040 (1995).

[77] D. L. Maslov, Transport through dirty Luttinger liquids connected to reservoirs, Phys. Rev. B **52**, R14368 (1995).

[78] D. L. Maslov and M. Stone, Landauer conductance of Luttinger liquids with leads, Phys. Rev. B **52**, R5539 (1995).

[79] J. Vidal, D. Mouhanna, and T. Giamarchi, Correlated fermions in a one-dimensional quasiperiodic potential, Phys. Rev. Lett. **83**, 3908 (1999).

[80] J. Vidal, D. Mouhanna, and T. Giamarchi, Interacting fermions in self-similar potentials, Phys. Rev. B **65**, 014201 (2001).

[81] M. Papaj, Spectroscopic signatures of excitonic order effect on quantum spin Hall edge states, arXiv:2310.08810.

[82] C. Zhang, T. Zhu, T. Soejima, S. Kahn, K. Watanabe, T. Taniguchi, A. Zettl, F. Wang, M. P. Zaletel, and M. F. Crommie, Local spectroscopy of gate-switchable Chern insulating states in twisted monolayer-bilayer graphene, Nat. Commun. **14**, 3595 (2023).